

## White paper

# V1 Deep Dive Project

Reza Abbasi-Asl

*Scientist I, Allen Institute for Brain Science*

### Contributors:

Josh Larkin, Kevin Takasaki, Daniel Millman, Daniel Denman, Jerome Lecoq,  
Anton Arkhipov, Nathan W. Gouwens, Jack Waters, Marc Takeno, Nuno de Costa,  
R. Clay Reid, and Saskia E. J. de Vries

Aug 2019

## Table of Contents

<b>Abstract</b>	<b>3</b>
<b>Experimental methods</b>	<b>4</b>
<b>Stimuli</b>	<b>4</b>
<b>Imaging strategy</b>	<b>5</b>
<b>Analysis methods / evaluation metrics</b>	<b>5</b>
<b>Chapter one: Platform</b>	<b>7</b>
<b>Number of cells</b>	<b>8</b>
<b>Response properties to Locally sparse noise</b>	<b>10</b>
Examples of estimated receptive fields	10
Responsiveness to locally sparse noise and SNR	12
Population receptive fields	13
Distance of RF center from center of stimuli presentation	14
<b>Response properties to full-field and windowed gratings</b>	<b>16</b>
Example of single cell tunings	16
Responsiveness fraction	18
Orientation and direction selectivity indexes	18
Preferred direction	20
<b>Response properties to natural scenes and movies</b>	<b>21</b>
Reliability of responses	21
Lifetime and population sparseness	23
Responsiveness overlap	24
<b>Chapter two: Locomotion Analysis</b>	<b>26</b>
<b>Fraction running</b>	<b>26</b>
<b>Correlation between running with neural response</b>	<b>26</b>
<b>Running Modulation Index</b>	<b>27</b>
<b>Chapter three: Tiling and coverage</b>	<b>29</b>
<b>Distribution of ON and OFF subfields</b>	<b>29</b>
<b>Distance between RF centers as a function of distance between cells</b>	<b>30</b>
<b>Ongoing analysis</b>	<b>31</b>
<b>Acknowledgements</b>	<b>32</b>
<b>References</b>	<b>32</b>

## Abstract

Characterizing the relationship between neural function and connectivity is a central problem in visual sensory processing. In order to explore this relationship, we have recorded visual responses from pan-excitatory neurons within an 800X800 um region of primary visual cortex, spanning all visual layers from pia to white matter. This includes ~13,000 neurons per mouse in 4 mice total, collected from 250 2-photon and 7 3-photon calcium imaging planes spaced by ~16 um. This dataset will be used to examine the single-cell and population activity in primary visual cortex, and along with electron microscopic reconstruction from the same tissue, will serve as a valuable resource in studying the functional connectome in mouse cortex. A wide variety of visual stimuli were used to characterize neural responses, including drifting gratings, sparse noise, natural movies and natural images. We assessed multiple metrics, including receptive field profile, direction and orientation selectivity indices, reliability of response, and sparseness of response. Here, we describe these metrics as a function of depth and explore their heterogeneity.

# Experimental methods

## Stimuli

Visual stimuli were presented using the same monitor configuration as the Brain Observatory pipeline (de Vries et al. 2018). The one-hour imaging session consisted of a wide variety of visual stimuli, including full-field and windowed drifting gratings, locally sparse noise, natural scenes and natural movies. While these stimuli had similarities with those used in the Brain Observatory pipeline, they differed in several ways.

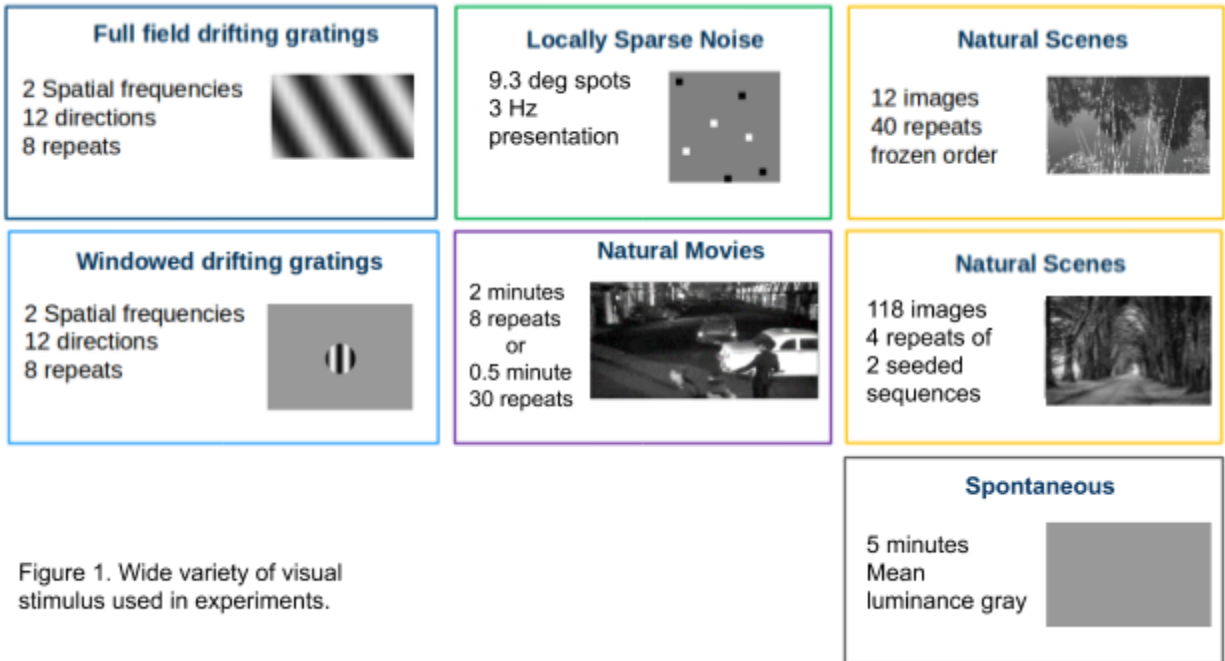
The full-field drifting gratings stimulus consisted of a drifting sinusoidal grating at a single temporal frequency (1Hz) and contrast (80%). The grating was presented at 12 different directions (separated by 30°) and at 2 spatial frequencies (0.04 and 0.08 cycles per degree). Each grating was presented for 2 seconds, followed by 1 second of mean luminance gray before the next grating. Each grating condition (direction & spatial frequency combination) was presented 8 times. Trials were randomized, with blank sweeps (i.e. mean luminance gray instead of grating) intermingled.

The windowed drifting grating stimulus matched the full-field stimulus, with the key difference that the stimulus was restricted to a 30° diameter window. For each column, the position of the window was determined separately to align with the population receptive fields of imaged neurons.

The locally sparse noise stimulus consisted of white and dark spots on a mean luminance gray background. Each spot was a square 9° on a side. Each frame of this stimulus was presented at ~3Hz. While this stimulus is very similar to that used in the Brain Observatory pipeline, it is not the exact same stimulus.

Two natural scenes stimuli were presented. One consisted of 12 images (selected from those used in the Brain Observatory pipeline) presented in a frozen sequence, and repeated 40 times. The other consisted of the full 118 images from the Brain Observatory pipeline, presented 8 times total. The images were presented in a random order, but fixed with two different seeds. Each of the two seeded sequences was presented 4 times. The images were presented at 3 Hz.

The natural movies stimulus for mice *slc2*, *teto1* consists of 3,600 frames (with 30Hz frame rate) and presented 8 times. For *slc4* and *slc5*, the stimulus consists of 900 frames and presented 30 times. For natural movies, to avoid confusion, we only present the results for mouse *slc2*, which is selected for EM reconstruction. Figure 1 summarizes the details of stimulus presentation.



## Imaging strategy

In order to record the full 800 X 800 X ~800  $\mu\text{m}$  volume, both 2-photon (2P) and 3-photon (3P) imaging are used. 5 columns of 5 stacked volumes are imaged using the 2P Deepscope (Lui et al. 2018) to cover the top 800 X 800 X ~500. Figure 2 shows the details of formatting of columns and volumes. Each volume imaged 6 planes, separated by 16  $\mu\text{m}$ , simultaneously, at 37 fps such that each plane is imaged at 6 Hz.. Each volume thus spans 80  $\mu\text{m}$ . Four columns create a grid covering 800 X 800  $\mu\text{m}$ , while the 5<sup>th</sup> column captured the center of the entire 800 $\mu\text{m}$ <sup>3</sup> Volume. The center column is extended to white matter using 3P imaging. The 3P imaging covers a total of at least 175  $\mu\text{m}$  across 6 planes or more (different across mice), imaged independently, separated by 25  $\mu\text{m}$  each.

## Analysis methods / evaluation metrics

The pre-processing is performed using the standard LIMS pipeline as used for the Visual Coding 2P dataset. This includes motion correction, segmentation, demixing, neuropil subtraction, ROI filtering, and df/f calculation. Except the receptive field mapping, all the other analysis is performed using the df/f traces. For the receptive field mapping, events detected by L0-penalized algorithm are used to achieve a more accurate estimation of receptive field.

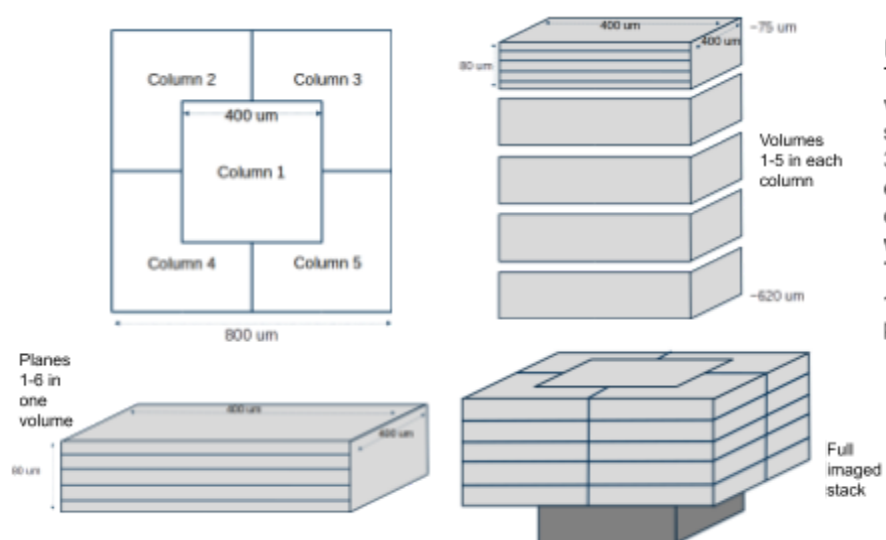


Figure 2. The imaging technique. To yield 800 X 800 X ~500  $\mu\text{m}$  volume for 2P, 5 columns of 5 stacked volumes are imaged. With 37 fps imaging for each volume, each plane is imaged at 6 Hz. The center volume is extended to white matter using 3P imaging. The 3P imaging covers a total of ~200  $\mu\text{m}$  total across at least 6 planes.

## Chapter one: Platform

In this chapter we present a survey the visual response metrics. Figure 3 shows the spatial organization of the cells recorded in one mice. Cells in the center column are colored in red and cell in surrounding columns are colored in white. Cell imaged by 3P are colored in purple.

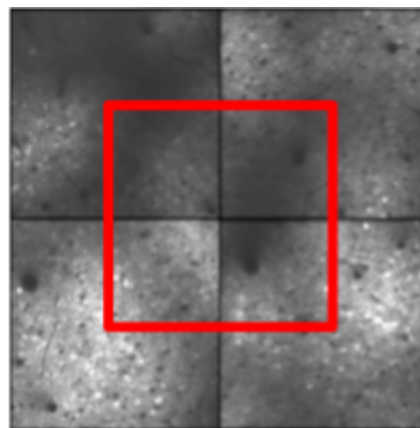
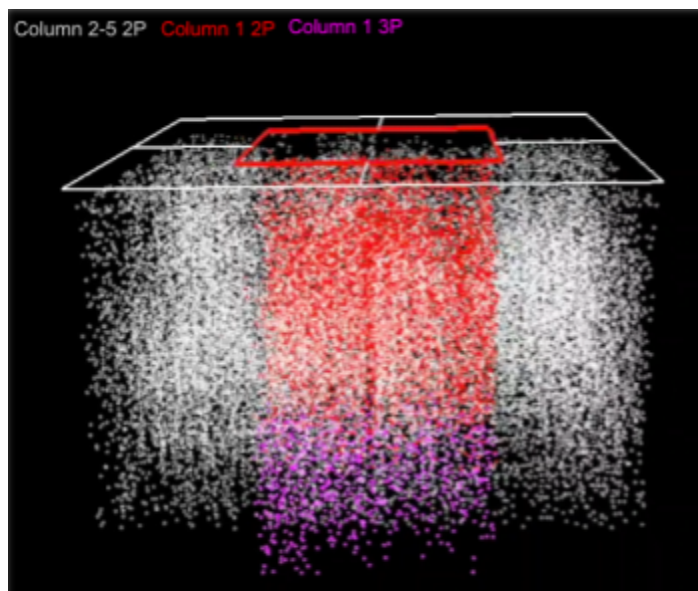


Figure 3: Recorded cells in mouse slc-4. Cells in center column are colored red. Cells in columns 2 to 5 are colored white. Cells recorded with 3-photon imaging are colored in purple.

Table 1 summarizes the four mice imaged for this project. Originally the plan was to image 5 mice, however, mouse Slc1 is excluded from the analysis because of a tissue damage that happened during imaging of this mouse.

Table 1 Relevant information for the 5 mice

No.	Mouse ID	Cre line	# valid cells total	# unique cells	Comments	Selected for EM
1	Slc2	Slc17a7;Camk2a;Ai94	12,836	9,365	Col.1 Vol.5 and Col.2 Vol. 1 failed pre-processing	**
2	Teto1	TetO;Camk2a	7,309	5,690	Col.1 Vol.2 and Col.2 Vol. 1 failed pre-processing	
3	Slc4	Slc17a7;Camk2a;Ai94	24,124	18,136	All volumes included	
4	Slc5	Slc17a7;Camk2a;Ai94	15,414	10,417	Col.2 Vol.5 failed pre-processing	
		Total	47,079	43,608		

## Number of cells

Figure 4 details the cell count as a function of depth, column and mouse ID. Note that some cells are imaged twice because of the overlap between column 1 and the other four columns. Figure 4A shows the total cells as a function of depth (for all mice and all columns), including all 5 columns. Figure 4.B, on the other hand, shows the unique cell count as a function of depth, where we only report number of cells in columns 2, 3, 4, and 5. Figure 4.C shows the number of total cells in each individual column. Figure 4.D shows the number of total neurons for each mouse, for each volume across all columns. The TetO mouse yielded many fewer neurons than Slc17a7, and this prompted more data to be collected from Slc17a7 mice.

For most of the analysis presented in this paper and unless noted, we only include cells in columns 2, 3, 4, and 5 to avoid duplicate cells (except for 3P cells which are only imaged in column 1). In the future, matching cells between column 1 and the surrounding overlapping columns could help to account for the duplication of neurons.

The 3P imaged cells are shown in yellow in Figure 4. We have used 3P imaging to only record cells in column 1 (center column) and thus there are fewer cells in the 3P compared to any other



depth. Also, note that 3P spans 5 planes over 200  $\mu\text{m}$  while others volumes span 6 planes over 80  $\mu\text{m}$ .

Signal to noise ratio (SNR) of the detected events for each cell is computed as:

$$SNR = 10 \log( \text{Mean}(P_{\text{Events}}^2) / \text{Var}(\text{Noise}) )$$

Where  $P_{\text{Events}}$  is the event magnitude. Note that we only use events for estimating receptive field and computing SNR and other analysis are based on  $dF/F$ . Figure 5 bottom panel shows the SNR of events as a function of depth. The median SNR increases with depth to 320  $\mu\text{m}$  where the highest SNR is achieved. Then the median SNR decreases with depth.

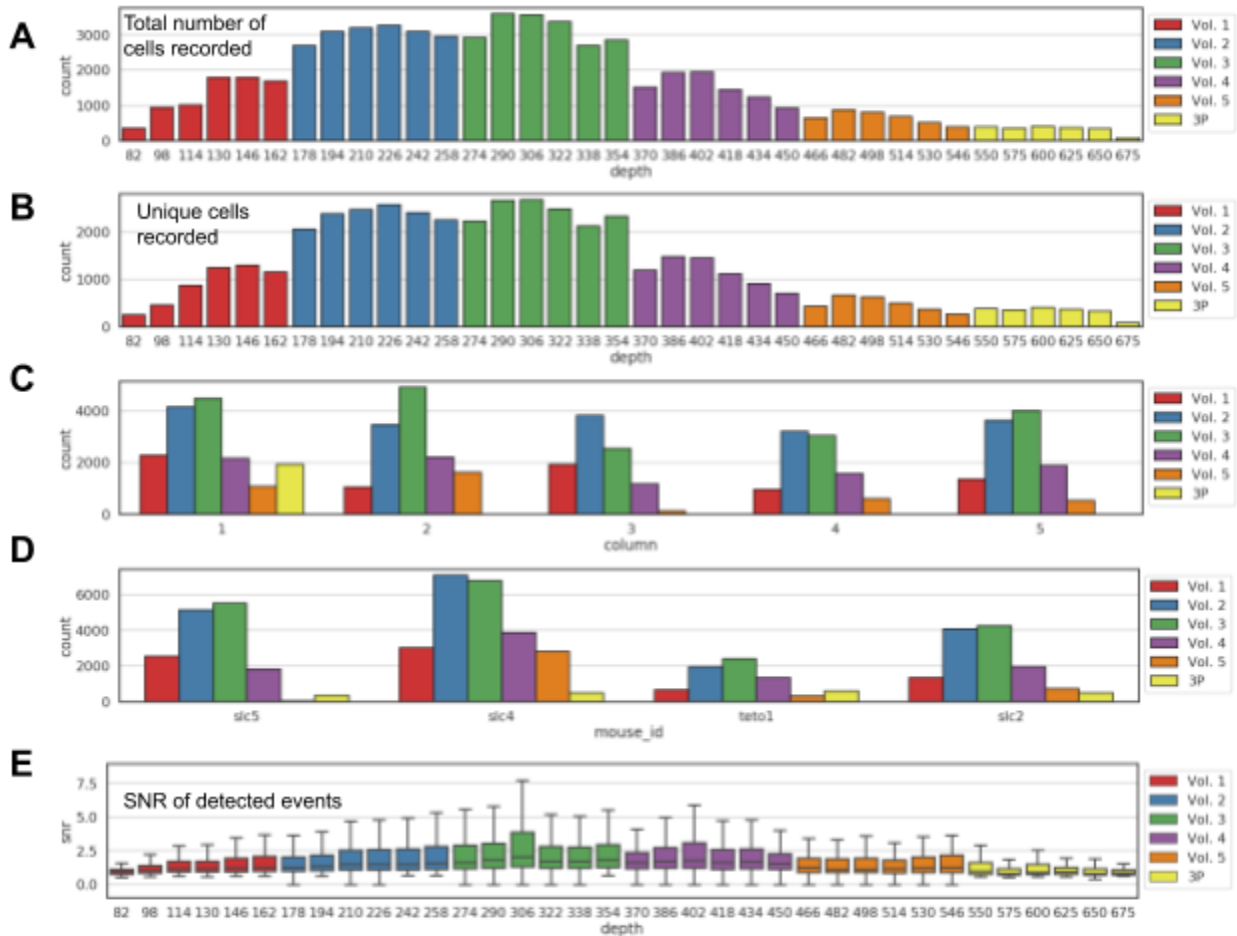


Figure 4. Cell count in the V1 column. A. Total number of imaged cells (marked valid through filtering process) recorded at each distinct depth for all mice and all columns. Color shows the volume that the planes are recorded simultaneously. B. Total number of unique cells as a function of depth. C. Total number of cells in each column. Same color code. D. Total number of cells for each mouse separated by volume. Same color code. E. Signal to noise ratio of detected events

## Response properties to Locally sparse noise

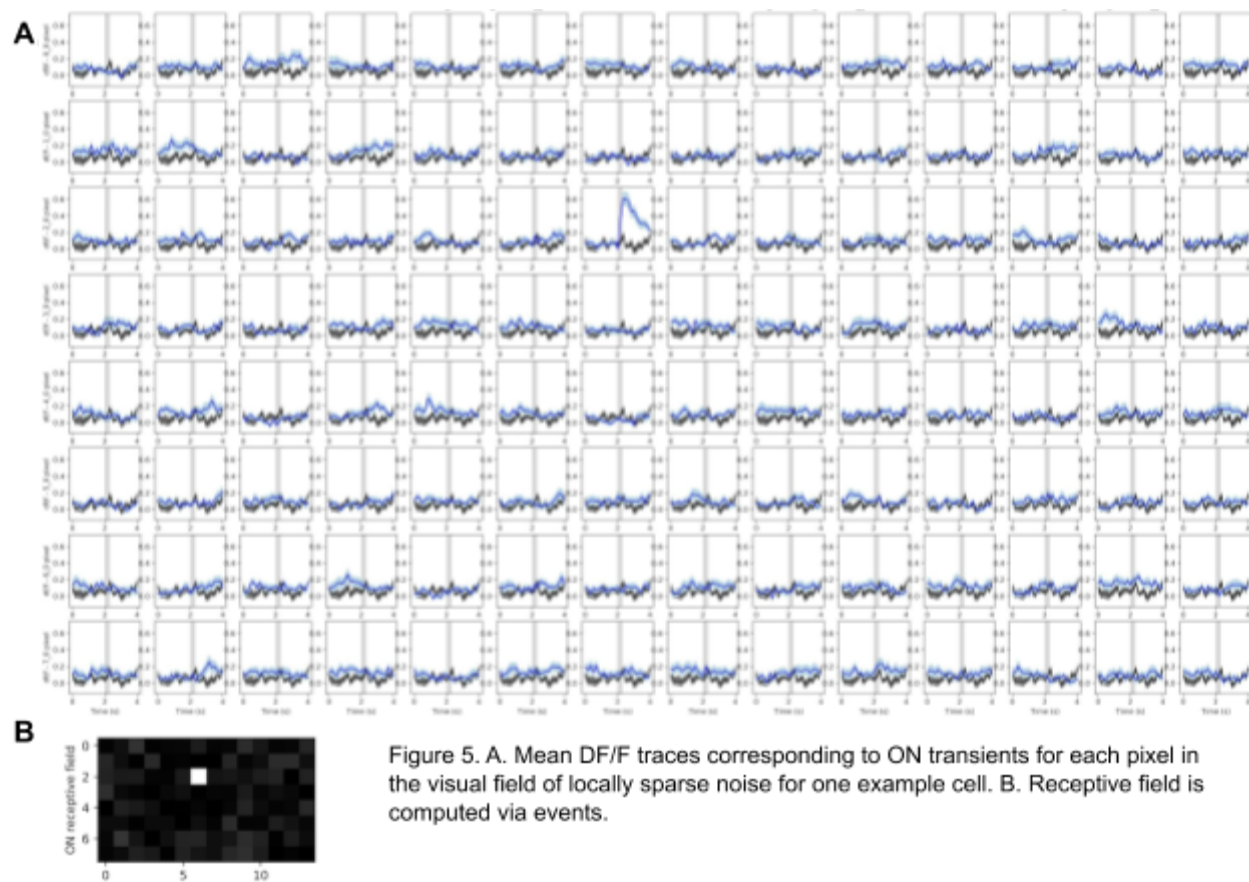
### Examples of estimated receptive fields

Figure 5 shows the mean  $dF/F$  traces corresponding to ON transients for each pixel in the visual field of locally sparse noise for one example cell. Here for one pixel, the average trace is significantly higher compared to spontaneous activity (shown in black).

To find the receptive field using the locally sparse noise stimulus, we calculated the the stimulus triggered average receptive fields. Figure 6 shows ON and OFF subfields for three example cells. All the receptive field analysis are performed over detected events from calcium imaging recordings via L0-penalized event detection algorithm.<sup>1</sup>

---

<sup>1</sup> From “de Vries et al.”: The measured fluorescence traces that result from calcium imaging are noisy and slow reflections of underlying neural spikes. To properly estimate the functional properties of neurons we wish to infer their instantaneous activity based on their measured fluorescence traces. A recent paper demonstrated a fast algorithm for finding the exact L0-penalized solution for the event detection problem and showed that the L0-penalized solutions typically outperform L1-penalized solutions in the detection of spikes from fluorescence traces. This L0-penalized algorithm forms the basis for our event detection pipeline. Jewell et al.'s L0 deconvolution software is publicly available at <https://jewellsean.github.io/fast-spike-deconvolution/>. As we show below, low firing rate activity such as isolated spikes is difficult to detect in calcium signals, so we refer to this as “event” detection.



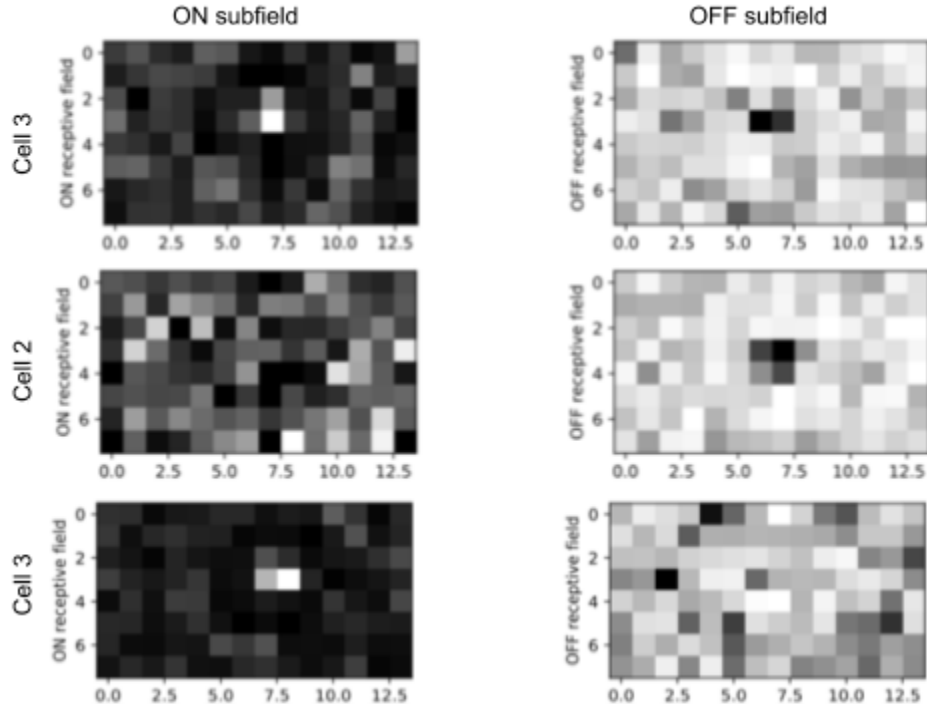


Figure 6. On and OFF subfield for three example cells. Left and right columns correspond to ON and OFF subfields, respectively. Cell 1 has clear ON and OFF subfields. Cell 2 and cell 3 have clear OFF and ON subfields respectively.

## Responsiveness to locally sparse noise and SNR

The responsiveness fraction to locally sparse noise (LSN) as a function of depth is shown in Figure 7. A cell is considered responsive to LSN if there is at least one pixel in chi-square test with a p-value less than  $0.05^2$ . We believe this is a conservative estimate of receptive fields. The maximum responsiveness fraction is achieved in 306  $\mu\text{m}$  with more than 40 percent of cells

<sup>2</sup> From “de Vries et al.”: For the statistical test to determine the presence of a receptive field, we performed a chi-square test to assess whether there was a significant response at each location to the locally sparse noise stimulus. For each location, we considered a 7x7 grid of locally sparse noise pixels centered on that location. The null model for this test was defined by assuming that a neuron lacking a receptive field has equal probability of producing a response regardless of the location and luminance (i.e. black or white) of the spots displayed on the screen on any given trial. In contrast, a neuron has a statistically significant receptive field if there is a deviation beyond chance from responsive trials occurring with equal probability across all spot locations and luminances. Chi-square tests for independence were performed for each neuron and for each location using the number of responses to quantify the dependence of responsive trials on the stimulus

responsive to locally sparse noise. The gap between volumes is possibly due to different sessions on different days. Overall, there are fewer significant receptive fields than expected (for comparison 90% of Slc17a7;Camk2a;Ai93 neurons imaged in the Brain Observatory pipeline in V1 had significant receptive fields using the same analysis and criteria (de Vries et al., 2018). It is possible that the lower fraction of responsive neurons found here is a result of the lower imaging rate (6 Hz vs 30 Hz). More work on the receptive field calculation and responsiveness criteria should be done in the future.

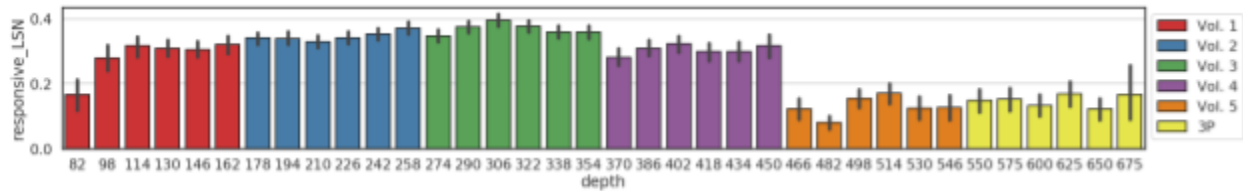


Figure 7. Response properties to locally sparse noise stimulus. A: Responsiveness rate to locally sparse noise stimulus as a function of depth.

## Population receptive fields

Figure 8 and 9 show the population receptive fields for ON and OFF subfields respectively. In each figure, the RFs are separated for each column and mouse, and include all 2P volumes. The red circle shows the location of the center of the stimulus for the windowed grating stimuli. For the majority of imaged columns, the population receptive field is well aligned with the stimulus presentation coordinates. Additionally, for most of the columns (with the exception of mouse Teto1, column3), the majority of cells have receptive fields that are far from the edge of the monitor.

More analysis regarding the distance between RF centers for individual cells and the windowed grating stimulus is presented in the next section .

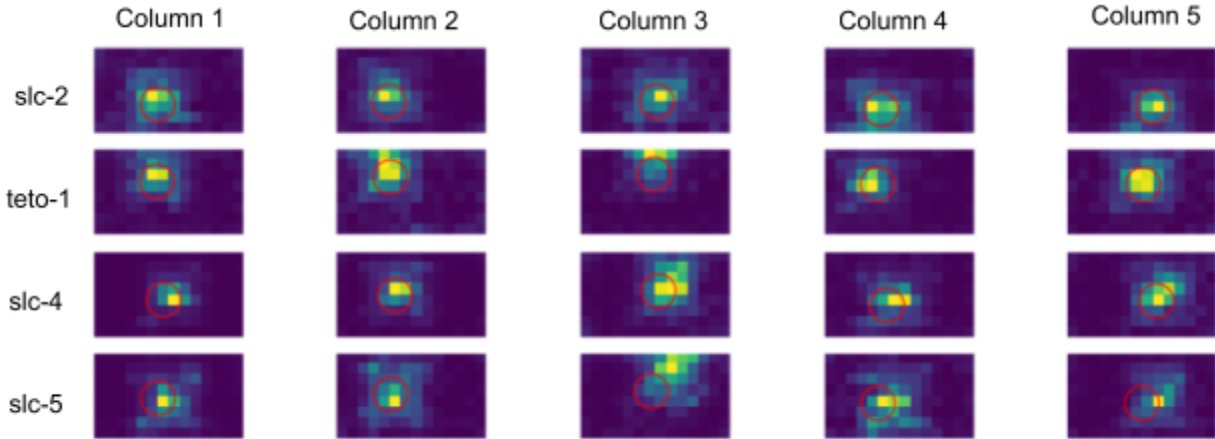


Figure 8. Population receptive fields for ON subfields for each column and each mouse.

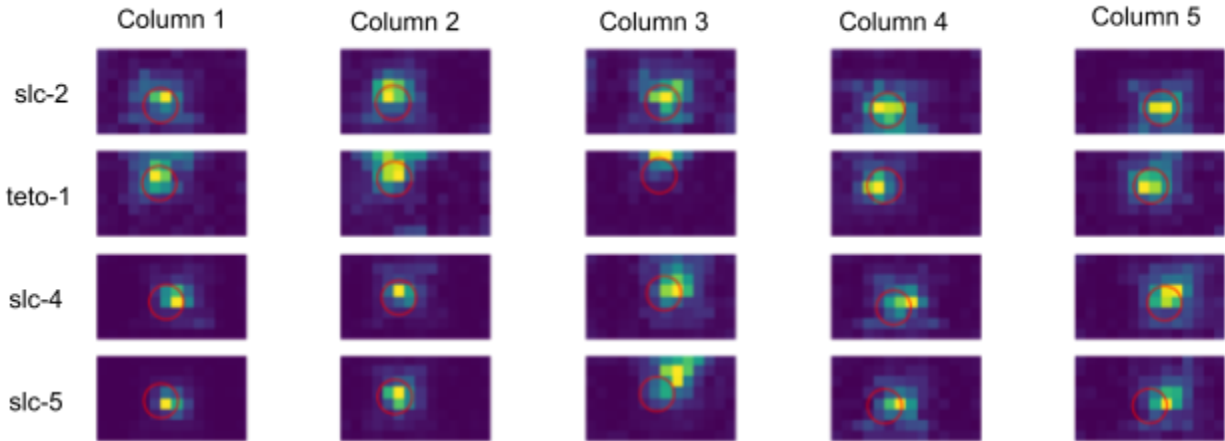


Figure 9. Population receptive fields for OFF subfields for each column and each mouse.

### Distance of RF center from center of stimuli presentation

To study the distance of the RF centers from the center of the windowed stimulus presentation we show the boxplots of distances for the center column in Figure 10. The center of the RF was estimated by identifying the 9.3 degree pixel in the receptive field with highest and lowest intensity for ON and OFF subfields, respectively. In future, we plan to improve our estimate of the center via fitting a Gaussian to the estimated RF. Top two panels in Figure 10 show the boxplots of distance for ON and OFF subfields as a function of depth. The red dashed line shows the edge of window circle at 15 degrees radius. From this we find that the median distance is at the edge of the window, and thus over half of the neurons have receptive fields

centered outside the windowed stimulus. A more detailed approach to receptive mapping, i.e. estimating the center from a gaussian fit, could improve these numbers somewhat. Bottom panels show the scatter plot and kernel density estimate comparing the distance for ON and OFF subfields. The distance is slightly lower for OFF subfields compared to ON subfields. Only cells from column 1 are included in these analyses. Most of 3P cells fall outside of the windowed grating.

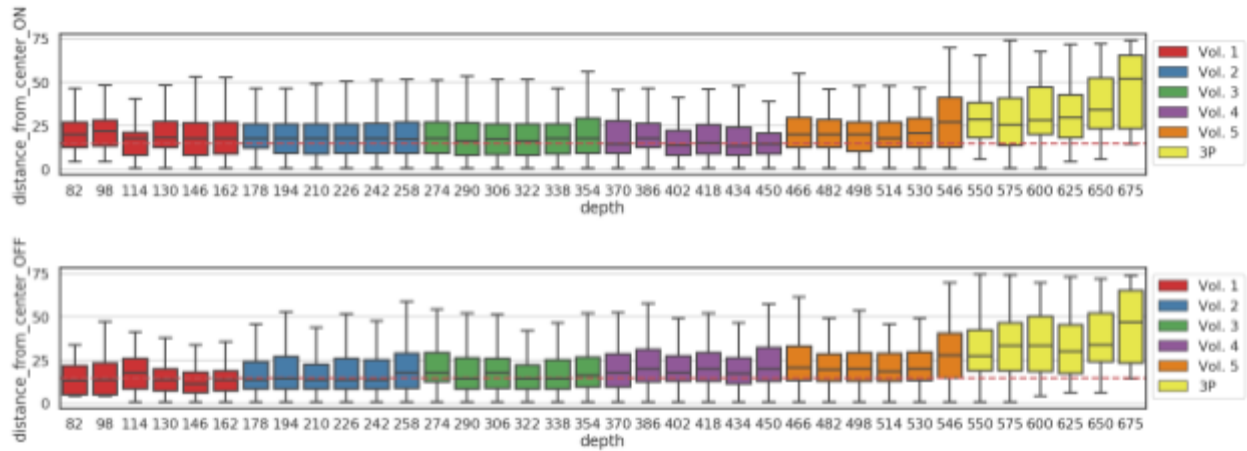


Figure 10. Distance of the RF center from center of stimulus presentation (in degrees) for cells in center column. Top two panels show the boxplots of distance for ON and OFF subfields as a function of depth. The red dashed line shows the edge of window circle at 15 degrees. Bottom panels show the scatter plot and kernel density estimate comparing the distance for ON and OFF subfields. The distance is slightly lower for OFF subfields compared to ON subfields. Only cells from column 1 are included in these analyses.

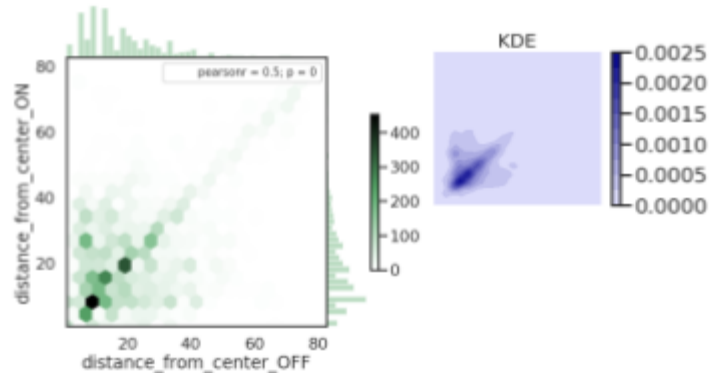


Figure 11 shows the portion of cells that have the center of their ON or OFF subfields inside the window for windowed gratings stimuli. The radius of window is 15 degrees. Only cells responsive to locally sparse noise are included in this analysis.

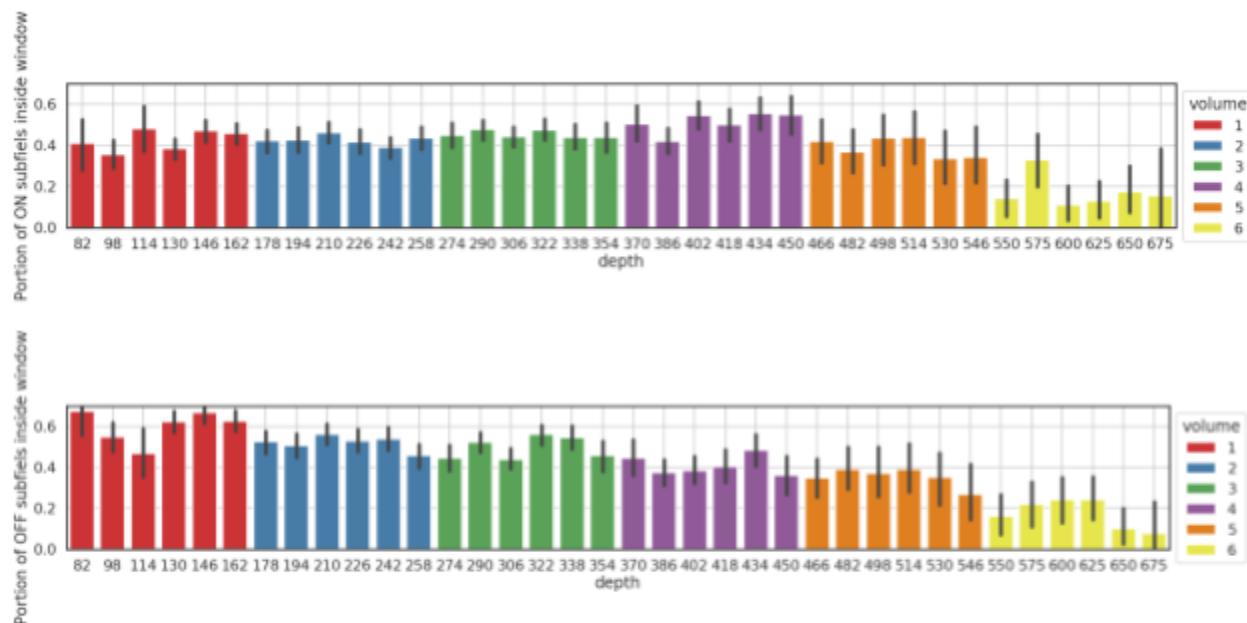


Figure 11. Portion of ON and OFF subfields that are inside the window for windowed gratings stimuli for cells in the center column. Only cells that are responsive to locally sparse noise are included.

## Response properties to full-field and windowed gratings

### Example of single cell tunings

Figure 12 shows tuning properties to both full field and windowed gratings for two example cells. For cell 1, responses to windowed gratings are much stronger (with a factor of 5) compared to responses to full-field gratings. Not all cells show the same profile. Cell 2 in Figure 12 shows a cell with relatively high responses for both windowed and full field gratings.



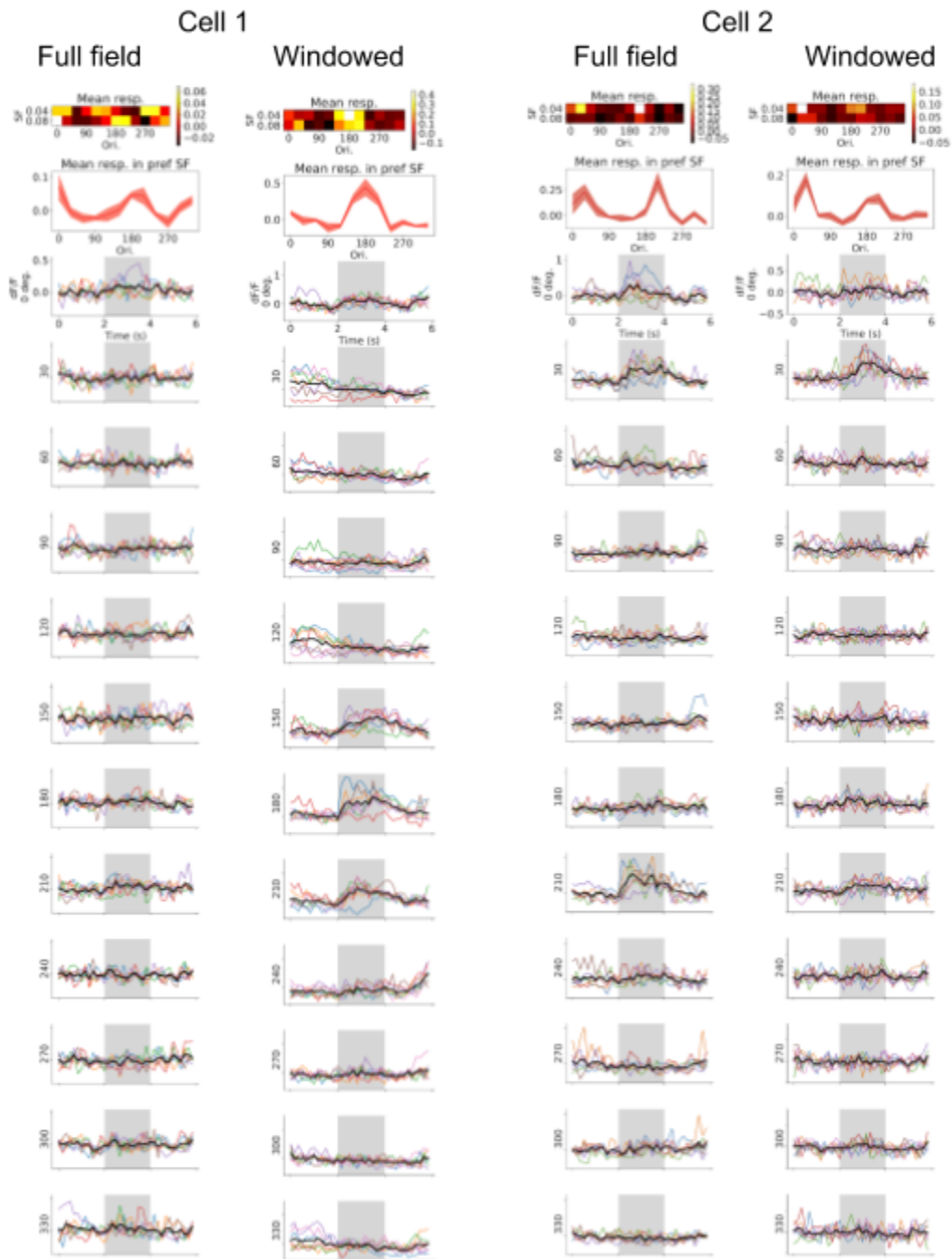


Figure 12. Response of two example cells to full field and windowed gratings. Top row shows the trial averaged response to each direction and spatial frequency. Second row shows the direction tuning profile for preferred spatial frequency. Remaining rows show the trial response to each direction. The average trace is shown in black. The presentation period is shown in gray. Note the difference in scaling between full-field and windowed responses.

## Responsiveness fraction

The responsiveness fraction to full-field and windowed gratings is demonstrated in Figure 13 for all the unique cells in four mice. A cell is considered responsive if it has significantly higher response from the spontaneous activity in more than half of the trials. The significance test is done by randomly sampling the 2-second windows from spontaneous activity 1000 times and comparing the average response to the stimulus presentation trials (p-value of 0.05). Overall 26% of cells responded to the full-field gratings whereas 30% responded to the windowed gratings. Overall, fewer cells respond to full-field gratings which is expected. This is particularly true for cells in depth less than 400  $\mu\text{m}$ . For cell deeper than 400  $\mu\text{m}$ , fewer cells respond to windowed gratings, likely reflecting the fact that many cells are not perfectly centered for the windowed stimulus in these planes.

The responsiveness ratio of for full-field gratings remains relatively flat across depth for 2P planes. Unlike the ratio for windowed gratings which achieve its maximum at 146  $\mu\text{m}$  and decreased for deeper planes.

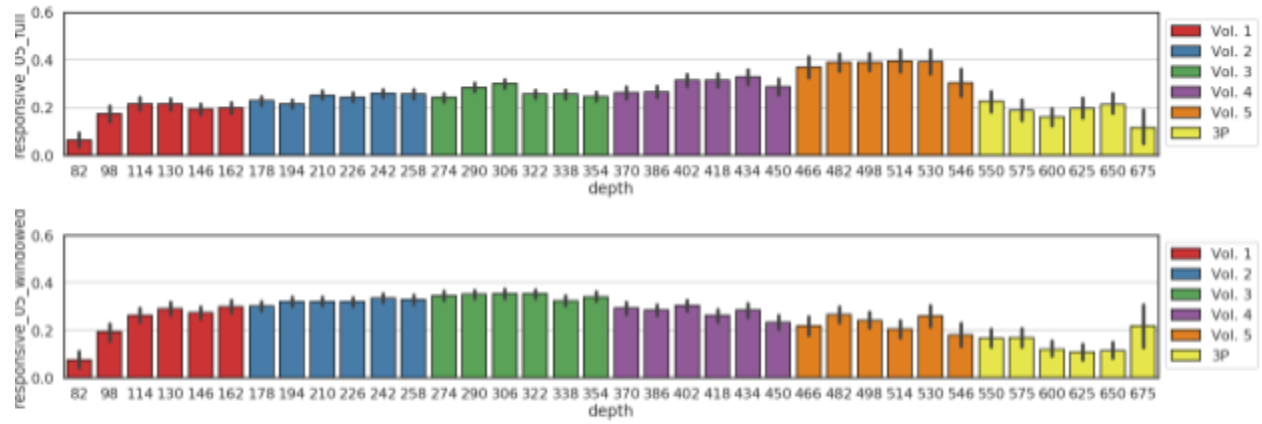


Figure 13. Responsiveness ratio to gratings for all the unique cells in four mice. Top panel: Barplots of responsiveness ratio to full-field grating. Bottom panel: Barplots of responsiveness ratio to windowed gratings. A cell is flagged responsive if it has significantly higher response from the spontaneous activity in more than half of the trials. The significance test is done by randomly sampling the 2-second windows from spontaneous activity for 1000 times and comparing the average response to the stimulus presentation trials.

## Orientation and direction selectivity indexes

Direction selectivity was computed from mean responses to drifting gratings, at the cell's preferred spatial frequency as:

$$g_{DSI} = (R_{pref} - R_{null}) / (R_{pref} + R_{null})$$

where  $R_{pref}$  is a cell's mean response in its preferred direction and  $R_{null}$  is its mean response to the opposite direction. Orientation selectivity was computed as:

$$g_{OSI} = |(\sum R_{\theta} e^{2i\theta}) / (\sum R_{\theta})|$$

where  $\theta$  is the orientation of grating movement and  $R_\theta$  is the mean response to that orientation.

Figure 14 shows the orientation selectivity index (OSI) and direction selectivity index (DSI) for both full-field and windowed gratings for all unique cells responsive to gratings.

Median of both OSI and DSI increased by depth up to 320  $\mu\text{m}$  and then decreased for deeper planes. For 3P planes, both DSI and OSI are relatively higher compared to volume 5. This might be due to differences in imaging techniques and higher quality of recording for 3P cells.

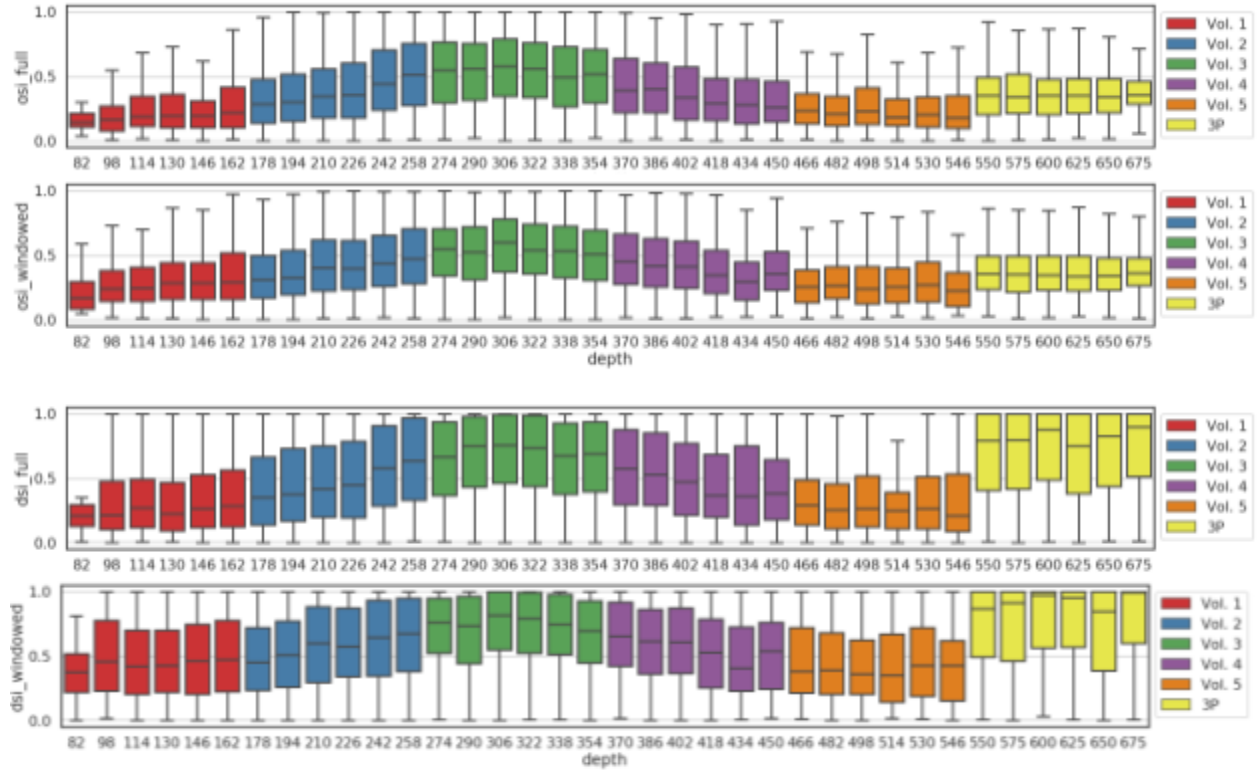


Figure 14. Orientation and direction selectivity indexes for full-field and windowed gratings stimuli for all the unique cells.

To further compare the OSI between full-field and windowed gratings, we show the distribution of OSI for each volume separately in Figure 15. All unique responsive cells are included. Both for the full-field and windowed gratings, the distribution for volume 3 is skewed toward higher values. For windowed gratings, volumes 2 and 4 have two mods in their distribution. This suggests that there are two groups of cells in these two volumes, one with high and the other with lower OSI. These two groups are separated based on the imaging depth i.e. some cells closer to volume 3 (layer 4) have higher OSI.

The correlation between OSI for full-field and windowed gratings is 0.54 for cell in the center column (Figure 15, right panel). The correlation is relatively high which is expected. Including all unique cells (without removing unresponsive cells), the correlation decreases to 0.27.

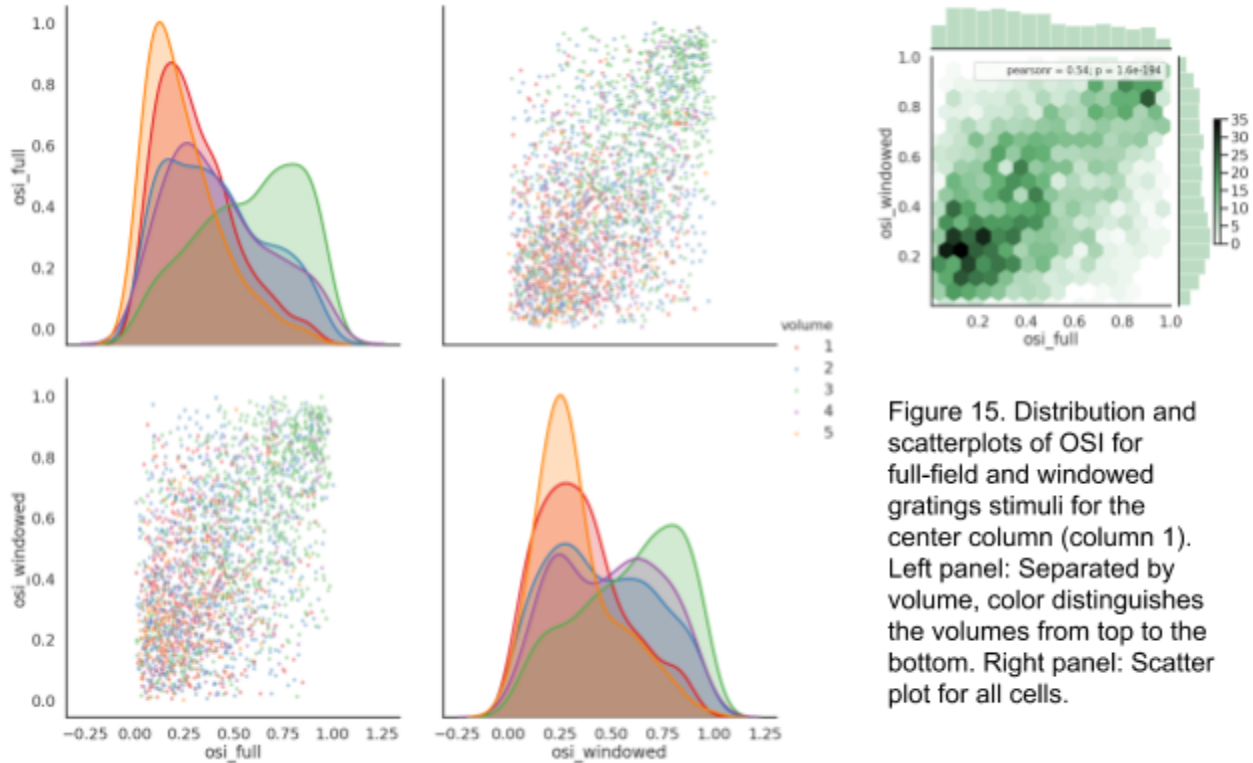


Figure 15. Distribution and scatterplots of OSI for full-field and windowed gratings stimuli for the center column (column 1). Left panel: Separated by volume, color distinguishes the volumes from top to the bottom. Right panel: Scatter plot for all cells.

## Preferred direction

To compare the preferred direction between full-field and windowed gratings, we first show the 2D kernel density estimation of the preferred direction for neurons that are responsive to both windowed and full-field gratings in Figure 16. The diagonal pattern is visible in this panel which implies the strong match between full-field and windowed responses for the majority of cells. The stripe at  $\pm 180^\circ$  reflects that we are comparing preferred direction and not all neurons are direction selective. The middle panel in Figure 16 shows the violin plots of distribution of difference between full-field and windowed preferred orientation as a function of depth. The distribution has the highest relative peak at zero degrees for many planes, with the stronger effect in volume 3. Bottom panel in Figure 16 shows the mean and standard error of the difference in preferred orientation. The mean is decreasing with depth until 322  $\mu\text{m}$  and then increases with depth.

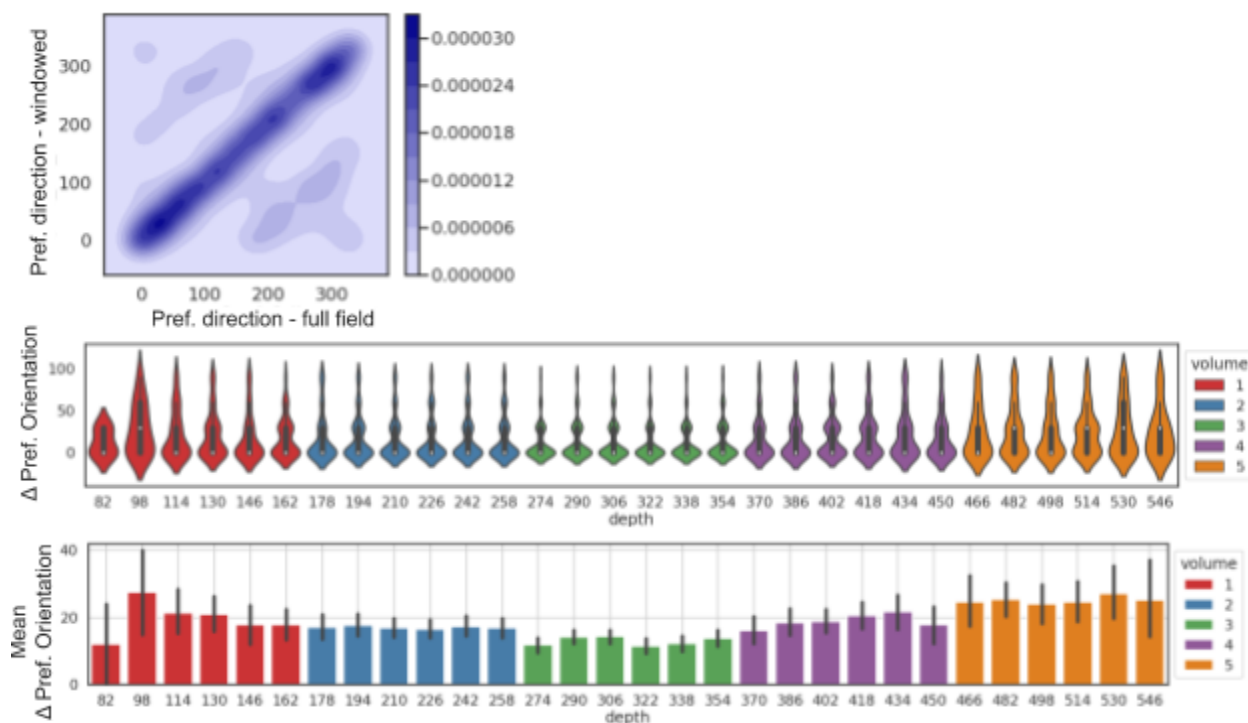


Figure 16. Comparing preferred orientation between full-field and windowed gratings. Top panel shows the kernel density estimation of the preferred orientation for all unique cells responsive to both full-field and windowed gratings. Middle panel shows the violin plots of distribution of difference between preferred orientation as a function of depth. Again all unique responsive cells are included. The distribution has highest relative peak at zero degree for planes in volume 3. Bottom panel shows the mean and standard error of the difference in preferred orientation. The mean is decreasing with depth until 322  $\mu\text{m}$  and then increases with depth.

## Response properties to natural scenes and movies

### Reliability of responses

The natural scenes and the natural movies present the same sequence of images across repeated trials. The natural scenes stimulus used in this section has only 12 images presented for 250 ms each but is repeated 40 times. Natural movies for the mouse *slc2* (which has been selected for EM reconstruction) has 3600 frames, with temporal correlations. But is only repeated 10 times.

Figure 17 shows the rasterplot of responses to natural movie and natural scene for two example cells. In response to natural movies, the top cell has reliable response to the 190th frame of the movie. The response to natural scenes is not as reliable. The bottom cell has reliable response to two frames.

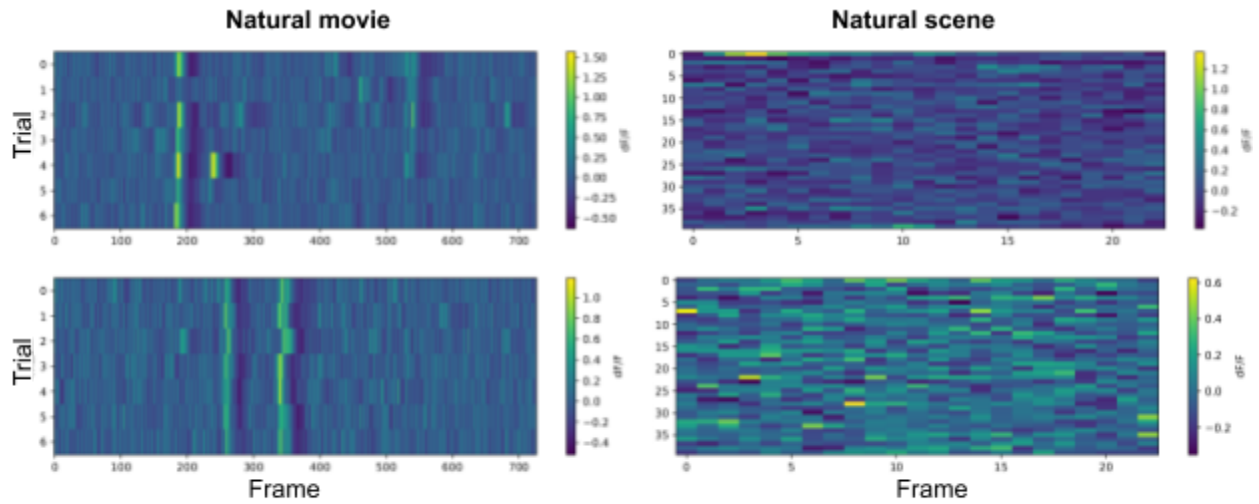
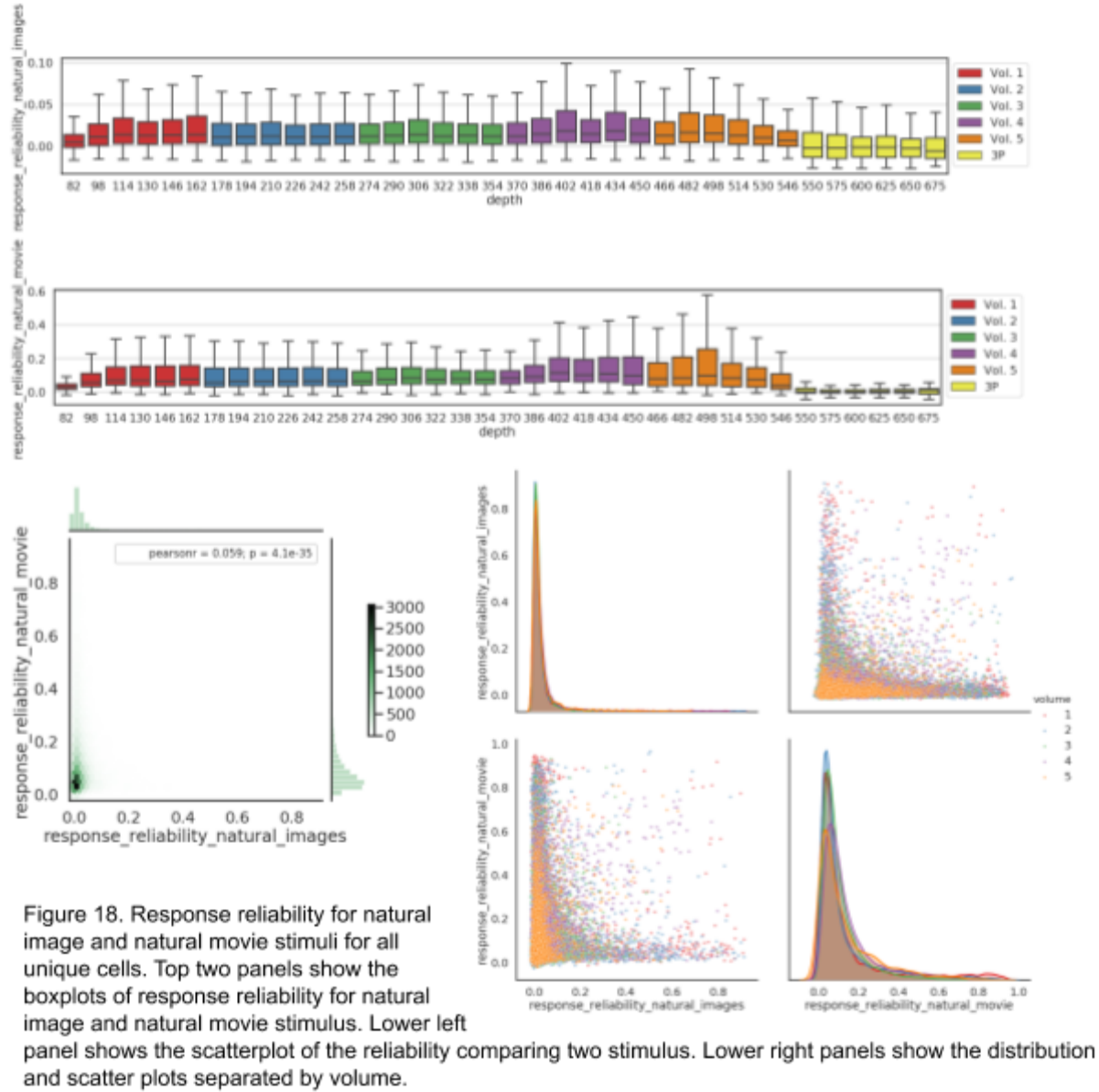


Figure 17. Response of two cells to natural scenes and natural movies.

To study the reliability of responses to natural scenes and natural movies, we compute the pairwise correlation coefficient between responses in different trials for each neuron and report the average correlation coefficient. No responsive criteria is applied here and all of the unique cells are included. Figure 18 shows the boxplots of such correlation values as a function of depth. Correlations are higher for the natural movies compared to natural images. For natural movies, the correlation iMean correlation is relatively higher around 176  $\mu\text{m}$  and 512  $\mu\text{m}$  for both natural images and movies. The scatterplots and distribution plots in Figure 16 doesn't show any considerable difference between different volumes.





## Lifetime and population sparseness

We have calculated the lifetime and population sparseness in neural responses to natural scenes. Note that the sparseness metrics are calculated using  $dF/F$  and for the natural scenes, there are only 12 images included here. The lifetime sparseness was computed using the definition in (Vinje et al., 2000) as:

$$S_L = \frac{1 - (\sum R_i)^2 / (N \sum R_i^2)}{1 - 1/N}$$

where  $N$  is the number of stimulus conditions and  $R_i$  is the response of the neuron to stimulus condition  $i$  averaged across trials. Population sparseness was computed with the same metric, but where  $N$  is the number of neurons and  $R_i$  is average response vector of neuron  $i$  to all stimulus conditions.

Overall, the responses are quite sparse. Top panel in Figure 19 shows the boxplots of lifetime sparseness as a function of depth for all of the unique cells. The lifetime sparseness slightly decreases by depth to ~350  $\mu\text{m}$  and increases by depth up to ~550  $\mu\text{m}$ . 3P planes are less sparse likely due to the quality of dF/F in 3-photon imaging. Bottom panel shows the boxplots of population sparseness as a function of depth for each volume. The median sparseness has the lowest value for volume 3 and increases in both directions (for shallower and deeper volumes).

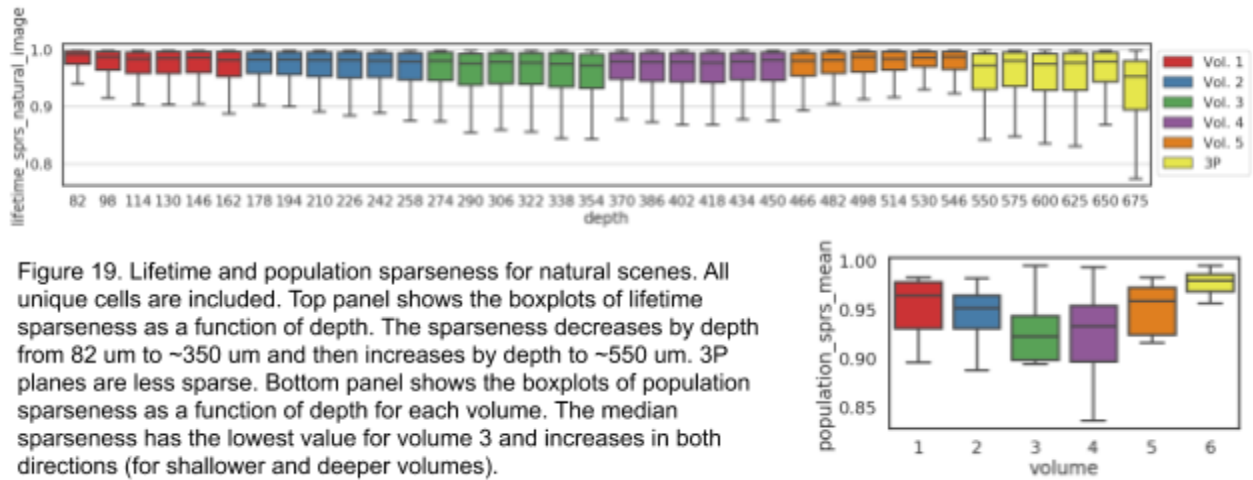


Figure 19. Lifetime and population sparseness for natural scenes. All unique cells are included. Top panel shows the boxplots of lifetime sparseness as a function of depth. The sparseness decreases by depth from 82  $\mu\text{m}$  to ~350  $\mu\text{m}$  and then increases by depth to ~550  $\mu\text{m}$ . 3P planes are less sparse. Bottom panel shows the boxplots of population sparseness as a function of depth for each volume. The median sparseness has the lowest value for volume 3 and increases in both directions (for shallower and deeper volumes).

## Responsiveness overlap

Figure 20 shows the responsiveness overlap between different stimuli. The heatmap shows the number of cells that respond to both stimuli divided by the total number of cells. For natural movie, the responsiveness is defined as having a response reliability higher than 0.05. Overall, there is very little overlap between the stimuli, with the highest overlap between the natural movie and the other stimuli (~30%), as well as full-field and windowed gratings (~15%). The low overlap of responses poses a challenge in many analyses comparing receptive field structure and effects of surround suppression.



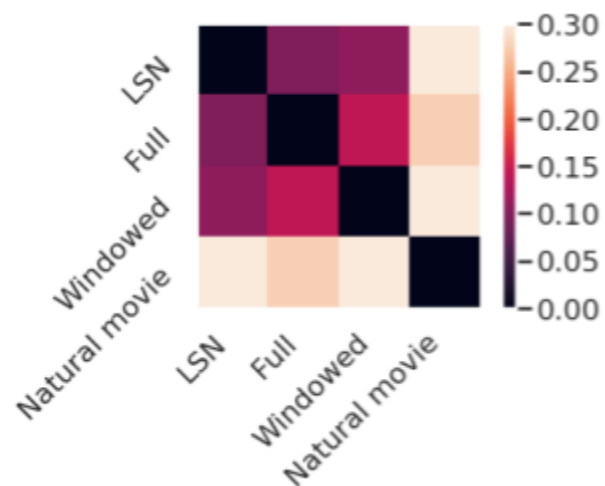


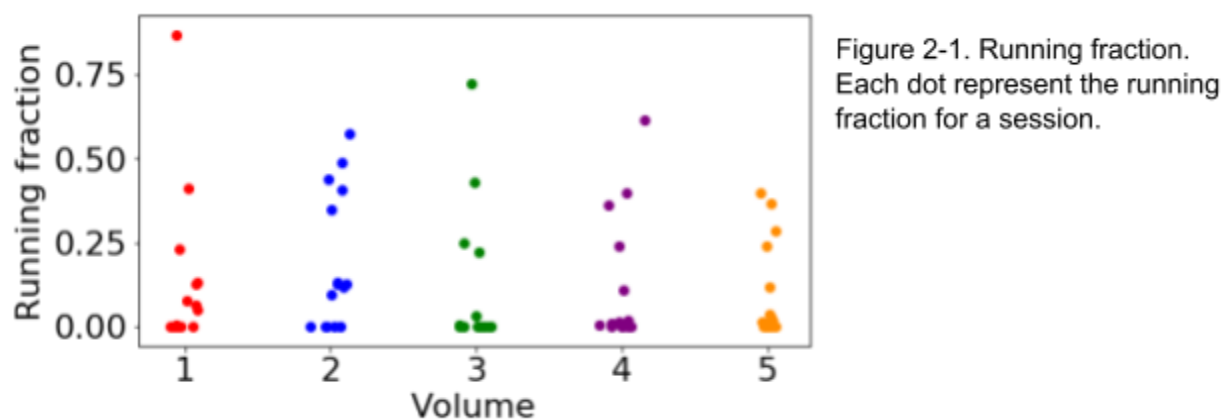
Figure 20. Responsiveness overlap between different stimuli. Numbers show the number of cells that respond to both stimuli divided by total number of cells. For natural movie, the responsiveness is defined as reliability higher than 0.05.

## Chapter two: Locomotion Analysis

In this section we study the locomotion and its effect on visually evoked neural response.

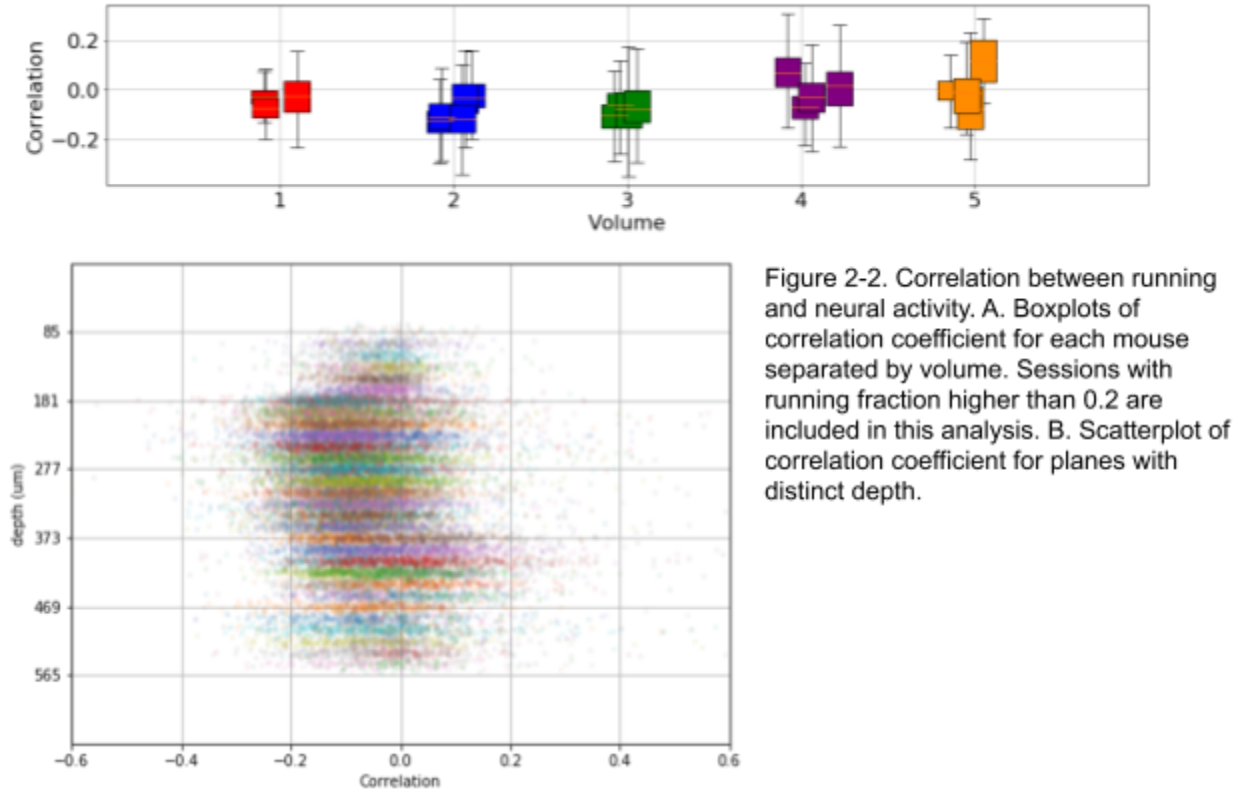
### Fraction running

First, we quantify the fraction of time that the mouse is running during an imaging session. Running is considered to be whenever the mouse has a speed greater than 1 cm/s. Running fraction is defined as total running time divided by the length of the session. Figure 2-1 shows the running fraction for all of the available sessions. Each dot represents a session in this plot.



### Correlation between running with neural response

Figure 2-2 top panel shows the boxplots of correlation coefficient between running and  $dF/F$  traces. The running speed is re-sampled to have the same temporal resolution as the  $dF/F$ . Only sessions with running fraction higher than 0.2 are included in this analysis. The median correlation increases for deeper volumes. To better visualize the distribution of correlation, we show the scatterplot of correlation coefficient for all the cells (in sessions with running fraction higher than 0.2) in Figure 2-2 bottom panel. Each color corresponds to a distinct plane. The majority of correlations have negative values. The correlation coefficient distribution remains relatively similar with depth up to 400  $\mu\text{m}$ . This is consistent with the observations by (DiPoppa et al. 2018). More importantly, we further observe that the correlation increases for deeper planes.



## Running Modulation Index

To quantify whether cells are modulated by the locomotion, we compute the running modulation index as:

$$Mod = C (R_{max} - R_{min}) / R_{max}$$

where  $C=1$  if  $R_{run} > R_{stat}$  and  $C=-1$  if  $R_{stat} > R_{run}$ . Figure 2-3 left panel shows the scatterplot of running vs. stationary responses and the color corresponds to running modulation index for mouse slc4. Only response to full field gratings are used in this analysis and all of the cells are included. The cells with higher running response compared to stationary response have higher running modulation index and colored in red. Similarly, the blue points show the cells with lower modulation index.

Figure 2-3, right panel shows the scatterplot of running modulation index as a function of depth for mouse slc4. Cells in each distinct imaging plane have different colors. Black bars show the median for modulation index for each column in that depth. The distribution is skewed toward

higher modulation index which implies most of the cells are positively modulated by running. For deeper planes, the distributions are less skewed toward positive values.

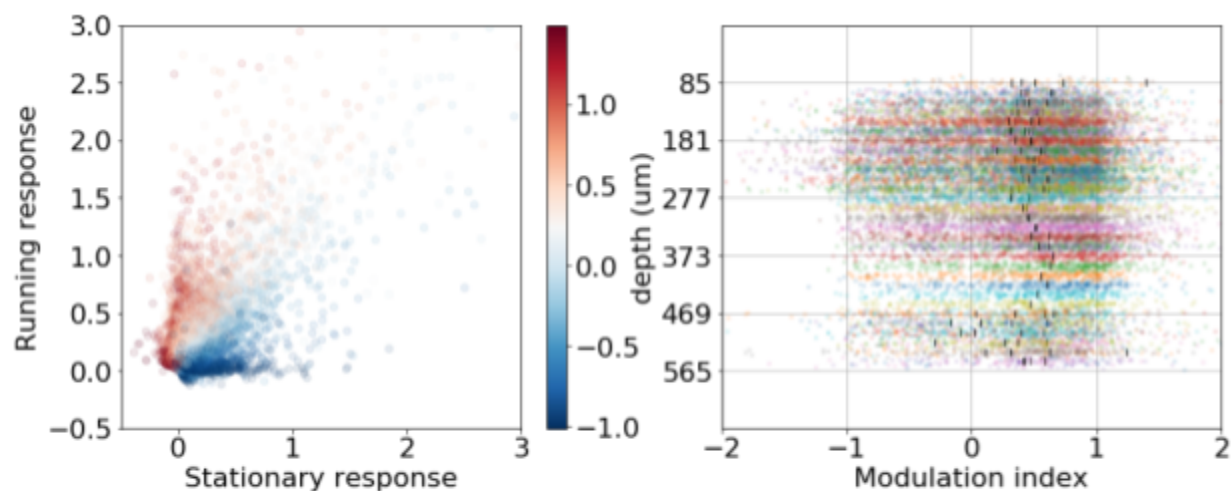


Figure 2-3. Running modulation index for mouse slc4. Left panel: scatterplot of running and stationary response colored with modulation index. Right panel: Running modulation index as a function of depth. Black bars correspond to median modulation index for each column.

## Chapter three: Tiling and coverage

In this chapter, we present further analysis for the location of receptive fields and its relationship with ROI locations and shape of the population receptive fields.

### Distribution of ON and OFF subfields

Figure 3-1 illustrates the distribution of ON and OFF subfields separately for each mouse and each volume. Only responsive cells from column 1 are included. Number of responsive cells in each volume is identified above the distribution. Number of level-sets is proportional to the number of cells in that mouse and volume. Overall, the distributions are not considerably different. For mouse slc-5, the distribution of OFF cells is less scattered in volume 1 and for deeper volumes, distributions get similar. Future modifications for estimating the receptive fields and particularly separate responsive criteria for ON and OFF subfields could help improve these analysis.

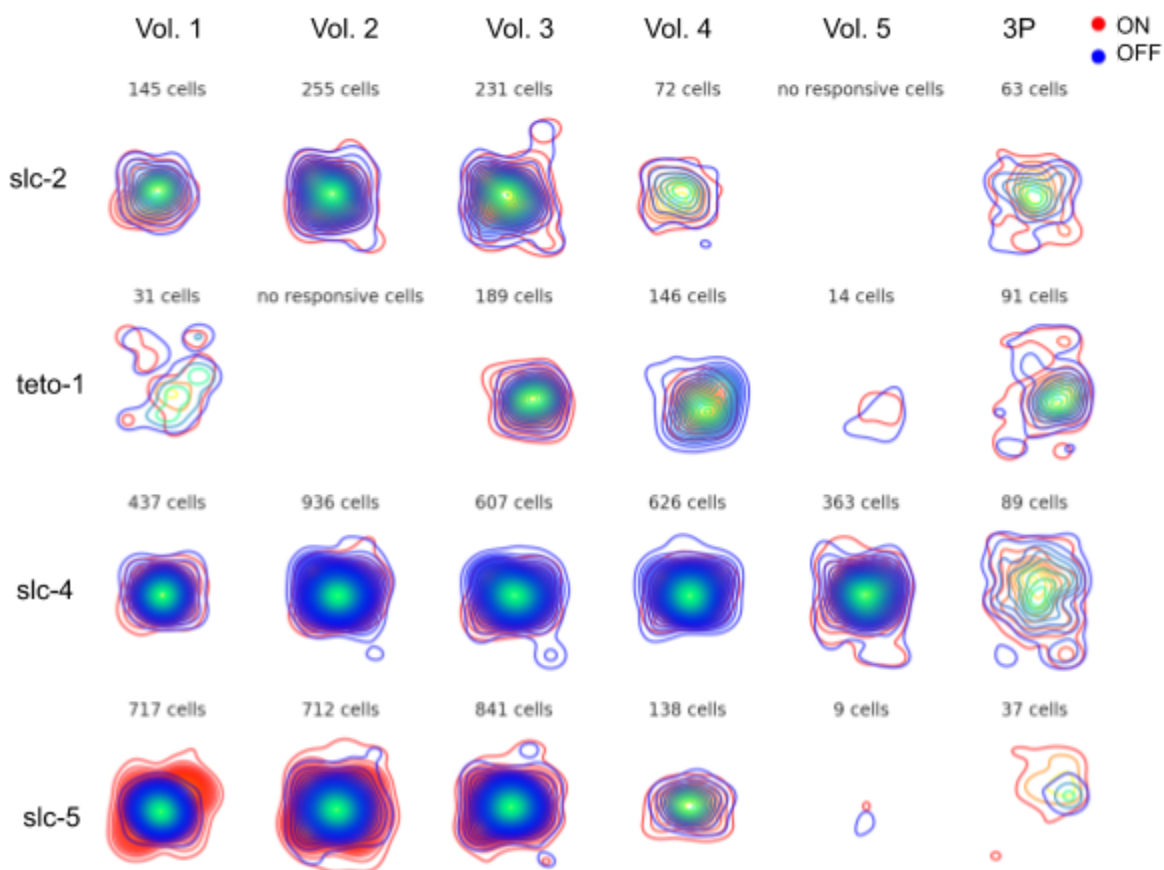


Figure 3-1. Population receptive fields for ON and OFF subfields.

## Distance between RF centers as a function of distance between cells

Figure 3-2, top two panels show the mean pairwise distance between ON and OFF subfields, respectively as a function of depth. The average pairwise distances were calculated within cells in each plane. Then barplots show the mean values from all the columns in all mice (that have responsive cells). The mean distances for ON and OFF are not significantly different. This is consistent with observations from Figure 3-1. The mean distances for ROI centers are also shown in Figure 3-2, bottom panel. As expected, the mean distance remains almost similar with depth.

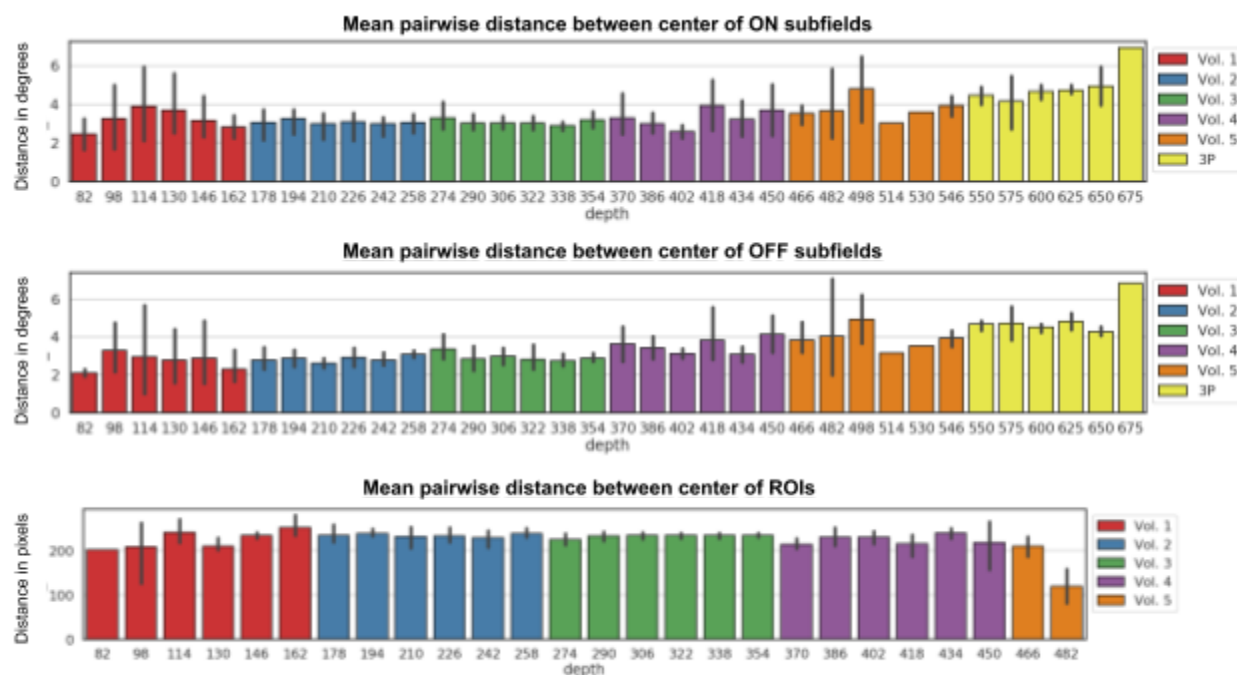


Figure 3-2. Mean pairwise distance between centers of ON subfields, OFF subfields and ROIs.

Furthermore, we calculated the correlations between pairwise distances of ON and OFF subfields. The barplots of the correlations is shown in Figure 3-3 top panel. The distances are highly correlated between ON and OFF subunits and correlation increases with depth.

We also calculated the correlation between pairwise distances of center of ON subfields and ROI centers. The barplots of correlations are shown in Figure 3-3 middle panel. Similarly, correlation between pairwise distances of center of OFF subfields and ROI centers is shown in Figure 3-3 bottom panel. OFF distances are slightly more correlated with ROI distances in volumes 2 and 3.

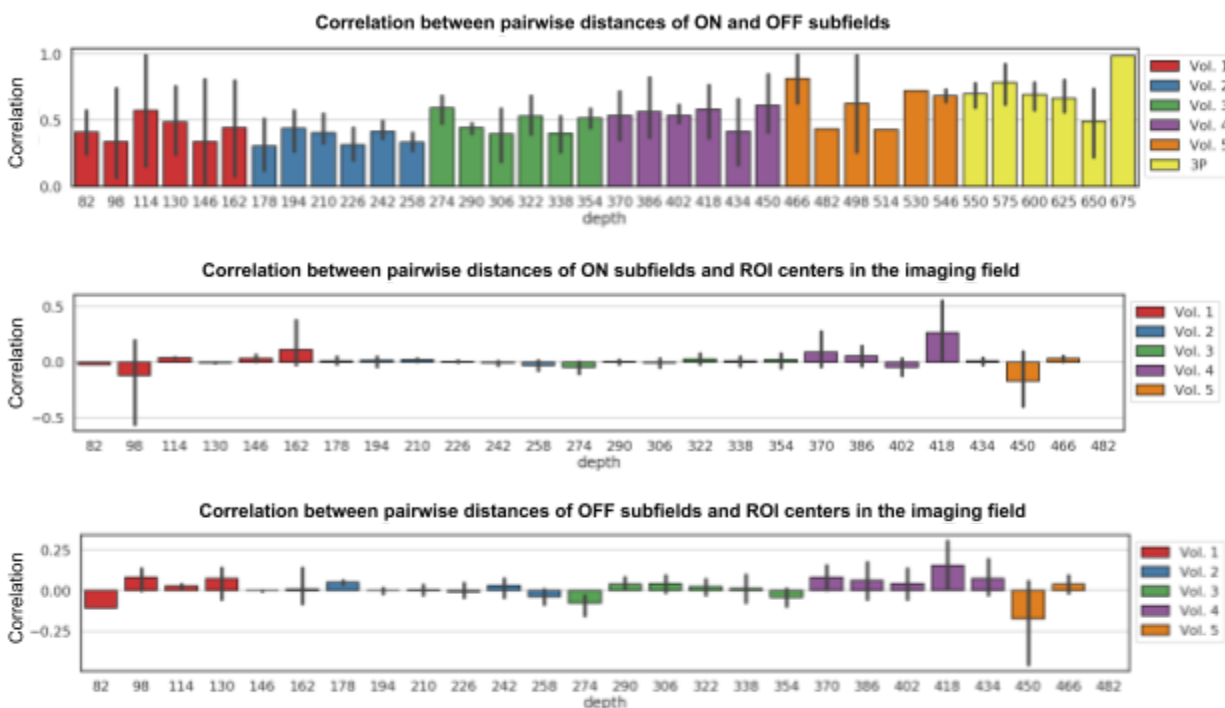


Figure 3-3. Correlation between pairwise distances of ON and OFF subfields and ROI centers in the imaging field

## Ongoing analysis

Some pieces of these analyses warrant more careful attention as we proceed.

- Receptive field analysis and responsiveness criteria. We believe our criteria might be too conservative and want to make sure we maximize what we can learn from these data regarding receptive field structures and tiling.
- 3P data. As this data modality is still relatively new, we want to spend a bit more time getting more eyes on this data to evaluate these responses.
- Matching cells between column 1 and the surrounding overlapping columns so that we can account for the duplication of neurons and still get the most information about the cells' responses.
- Signal and noise correlations and their properties as a function of distance between pairs of cells (per plane and per volume)
- Surround suppression analysis

## Acknowledgements

The authors would like to thank the Allen Institute founder, Paul G. Allen, for his vision, encouragement and support.

## References

- de Vries, S. E., Lecoq, J., Buice, M. A., Groblewski, P. A., Ocker, G. K., Oliver, M., ... & Roll, K. (2018). A large-scale, standardized physiological survey reveals higher order coding throughout the mouse visual cortex. *bioRxiv*, 359513.
- Dipoppa, M., Ranson, A., Krumin, M., Pachitariu, M., Carandini, M., & Harris, K. D. (2018). Vision and locomotion shape the interactions between neuron types in mouse visual cortex. *Neuron*, 98(3), 602-615.
- Liu, R., Ball, N., Brockill, J., Kuan, L., Millman, D., White, C., ... & Larkin, J. (2018). Multi-plane Imaging of Neural Activity From the Mammalian Brain Using a Fast-switching Liquid Crystal Spatial Light Modulator. *bioRxiv*, 506618.
- Vinje, W. E., & Gallant, J. L. (2000). Sparse coding and decorrelation in primary visual cortex during natural vision. *Science*, 287(5456), 1273-1276.